Estimating Geostrophic Shear from Seismic Images of Oceanic Structure*

KATY L. SHEEN AND NICKY WHITE

Bullard Laboratories, University of Cambridge, Cambridge, United Kingdom

C. P. CAULFIELD

BP Institute, and Department of Applied Mathematics and Theoretical Physics, University of Cambridge, Cambridge, United Kingdom

RICHARD W. HOBBS

Department of Earth Sciences, University of Durham, Durham, United Kingdom

(Manuscript received 19 October 2010, in final form 7 January 2011)

ABSTRACT

It is shown that geostrophic vertical shear estimates can be recovered from seismic (i.e., acoustic) images of thermohaline structure. In the Southern Ocean, the Antarctic Circumpolar Current forms a loop within the Falkland Trough before it flows northward into the Argentine Basin. Seismic profiles that cross this loop show the detailed structure of different water masses with a horizontal resolution of $O(10\ \text{m})$. Coherent seismic reflections are tilted in response to current flow around the Falkland Trough. Average slopes were measured on length scales that are large enough to ensure that the geostrophic approximation is valid (i.e., with a Rossby number <0.1). By combining shear estimates with satellite altimetric measurements and acoustic Doppler current profiles, geostrophic velocities can be calculated throughout the data volume. This technique for estimating geostrophic vertical shear from legacy seismic images yields useful information about the spatial and temporal variation of mesoscale circulation.

1. Introduction

A quantitative understanding of large-scale oceanic currents, which play a key role as global transporters of heat, salt, and nutrients, is an important ingredient of climatic modeling. Since direct measurement of current vectors throughout the oceanic volume is difficult and expensive to obtain, physical oceanographers often use the geostrophic approximation to estimate the baroclinic component of the velocity field. This estimate depends upon information about density distribution that is derived from conductivity–temperature–depth (CTD) measurements (e.g., Arhan et al. 2002; Sherwin et al. 2008). Beneath the sea surface, geostrophic calculations are limited by restricted spatial sampling.

Seismic reflection profiling is an important method for imaging thermohaline fine structure down to abyssal depths (e.g., Holbrook et al. 2003). During acquisition, acoustic energy generated by an array of air guns is reflected at boundaries within the water column where changes in acoustic impedance are produced by temperature and, to some extent, salinity variations (Sallarès et al. 2009). With careful signal processing, the resultant seismic (i.e., acoustic) image is a continuous vertical slice through an oceanic volume with a vertical and horizontal resolution of typically 10 m. Reflective surfaces are a reasonable proxy for true isopycnal surfaces because density variations are dominated by changes in temperature. A detailed description of seismic oceanography is given by Ruddick et al. (2009).

We describe how reliable geostrophic vertical shear estimates can be recovered from seismic images. These estimates can be used to reconstruct the geostrophic

* Department of Earth Sciences, University of Cambridge Contribution Number ESC.2157.

Corresponding author address: Katy Sheen, National Oceanography Centre, Southampton, University of Southampton Waterfront Campus, European Way, Southampton, SO14 3ZH, United Kingdom.
E-mail: k.sheen@soton.ac.uk

DOI: 10.1175/JTECH-D-10-05012.1

© 2011 American Meteorological Society

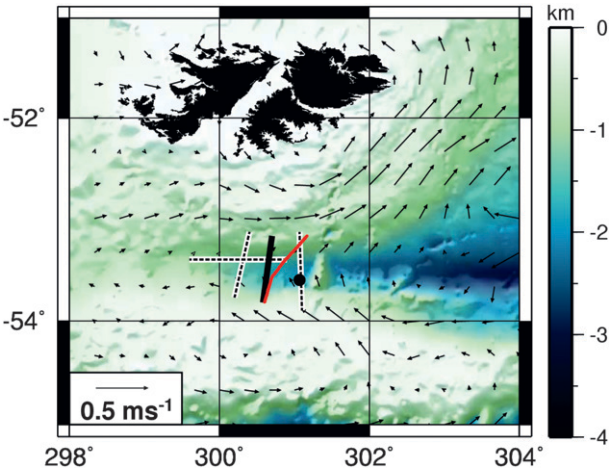

FIG. 1. Bathymetric map that shows altimeter-based geostrophic velocity field for 14 Apr 1993 (altimeter data produced by Segment Sol Multimissions d'Altimétrie, d'Orbitographie et de Localisation Précise/Multimission Altimeter Data Processing System (SSALTO/DUACS), distributed by Archiving, Validation, and Interpretation of Satellite Oceanographic data (AVISO) and Centre National d'Études Spatiales (CNES), and available online (at http://www.aviso.oceanobs.com/duacs/). Geostrophic velocity vectors (black arrows; note westward and eastward flow into and out of trough), location of seismic transect shown in Fig. 2a (solid black line), nearby CTD cast shown in Fig. 3 (solid black circle), additional seismic transects used in this study (black dashed lines), and ADCP profile acquired between 28 Feb and 1 Mar 2003 on cruise JR84 by Royal Research Ship (RRS) *James Clark Ross* (solid red line).

velocity field provided that a level of motion is known. Our example is taken from the Southern Ocean where the Antarctic Circumpolar Current (ACC) flows over the Falkland Plateau. Here, a suitable set of seismic images have been acquired and processed.

2. Falkland Trough Loop

The Falkland Trough is a bathymetric embayment that lies in the path of the ACC as it flows around the Falkland Islands toward the Argentine Basin (e.g., Arhan et al. 2002). Components of the ACC track westward along the southern edge of the Falkland Trough, looping around the shallow end of the trough before flowing eastward along its northern edge (Fig. 1). This current loop is clearly visible in the surface current pattern. Its position is tied to bathymetric slopes adjacent to the Malvinas Chasm. Satellite altimetric data demonstrate that the position of this loop is largely fixed on decadal time scales. The disposition of contourite deposits shows that the loop is a long-standing feature on the time scale of millions of years (Koenitz et al. 2008).

A loose grid of seismic reflection profiles cross this current loop (Fig. 1). The spatial resolution of these images is ~20 m and oceanic fine structure is well resolved. The configuration of the seismic experiment means that fine structure is smoothed over a period of ~30 min. Details of data acquisition and processing are described by Sheen et al. (2009) and briefly summarized in the caption of Fig. 2. A north–south profile is shown in Fig. 2a. This profile crosses the Falkland Trough where the direction of the current flow changes. Prominent tilted bands of coherent reflectivity are visible in the upper half of the image.

A seismogram, which shows reflectivity varying as a function of temperature and salinity, was computed for a CTD cast located adjacent to the acoustic image (Figs. 2a and 3). Qualitative comparison of this computed seismogram and the acoustic image suggests that the bright band of reflectivity at 0.5–1 km corresponds to stratified Antarctic Intermediate Water (AAIW). Beneath AAIW, an acoustically transparent layer corresponds to cooler and saltier Upper Circumpolar Deep Water (UCDW), which is denser and more homogeneous than AAIW. The shape of the boundary between these two water masses is convex, consistent with loopwise flow of both water masses inside the trough. A switch in the east–west component of water flow within the center of the trough is manifest by a marked reversal in slope at 53.5°S (cf. Figs. 4a and 4b). A continuous band of weak reflections is visible ~150 m above the seabed. The geometry of this band suggests that it is bathymetrically controlled. If so, it is possibly a thin layer of cold water that occasionally overflows into the trough by the mechanism described by Zenk (1981). On either side of the trough, undulating and disrupted reflections of AAIW are visible (e.g., Fig. 4c). The geometry of these disrupted reflections may be controlled by ageostrophic processes (e.g., breaking internal waves, boundary layer effects).

In Fig. 3, we compare depth profiles of the in situ vertical density gradient $\rho' = \Delta\rho/\Delta z$ with the acoustic impedance gradient calculated from the CTD cast $I' = \Delta I/\Delta z$. Correlation between ρ' and I' is good (with a correlation coefficient of $r = -0.72$), which suggests that we can use the geometry of seismic reflections to calculate rates of diapycnal mixing. First, vertical displacements of undulating reflections are measured to construct energy density spectra. A model that linearly combines the spectral behavior of both internal waves and turbulence is then used to estimate diapycnal diffusivity K along the profile (Sheen et al. 2009). The average calculated value of K is 10^{-4} m^2 s^{-1}. A marked increase in K toward the margins of the trough suggests that enhanced mixing associated with breaking of internal waves is occurring (Fig. 2b).

3. Geostrophic calculations

On longer length scales, we can calculate the horizontal component of the geostrophic velocity field,

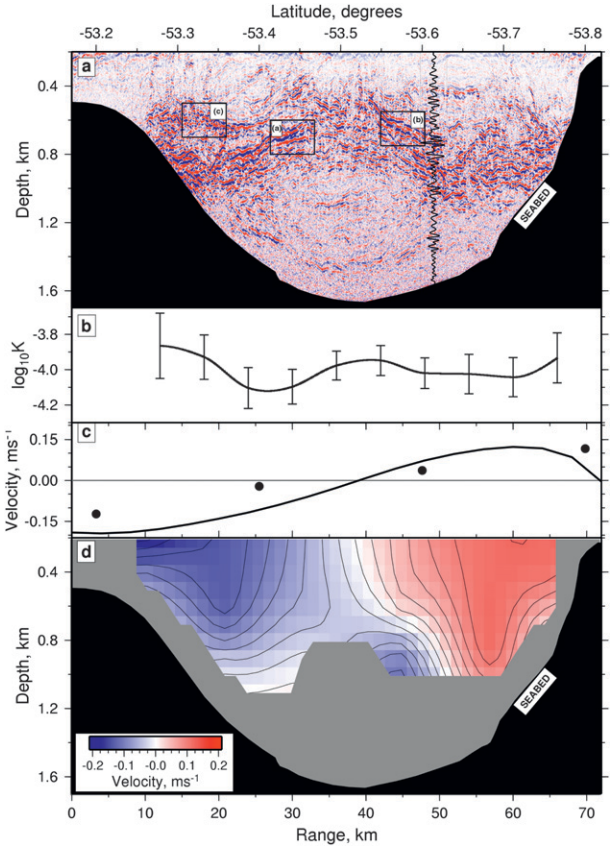

FIG. 2. (a) Seismic transect acquired by WesternGeco on 17 Apr 1993 using the *Akademik Shatsky*. It crosses the Falkland Trough where geostrophic velocity field switches direction (Fig. 1). See Sheen et al. (2009) for details of acquisition and signal processing. Positive (red lines) and negative (blue lines) reflections caused by temperature and salinity variations. Labeled boxes are enlarged in Fig. 4. Vertical wiggly line is the seismogram calculated from nearby CTD cast (see Figs. 1 and 3). (b) Variation in diapycnal diffusivity $\log_{10} K$ ($m^2\ s^{-1}$), averaged between 0.5- and 0.9-km depth (see Sheen et al. 2009 for further details). Error bars indicate one standard deviation. (c) Surface velocity variation along seismic transect (positive and negative values indicate westward and eastward flow, respectively). East–west component of geostrophic velocity calculated from satellite altimetric data every 1/3° (~20 km) for 14 Apr 1993 (solid black circles), east–west component of current velocity calculated from ADCP data that were averaged between 400- and 450-m depth (solid black line). Because ADCP data are 10 yr younger than seismic data, we have not carried out a tidal correction. (d) Velocity field estimated from spatial variation of geostrophic shear values calculated from seismic transect using methodology described in text. Calculated values were resampled on a 0.1 km × 0.1 km grid and smoothed. Contour lines plotted for every 0.02 m s^{-1}. Westward (red shading) and eastward (blue shading) flows are indicated, and the region either where seismic reflections are weaker than a specified noise threshold or where calculation breaks down due to boundary effects (gray shading; i.e., within 200 m of seabed) is shown.

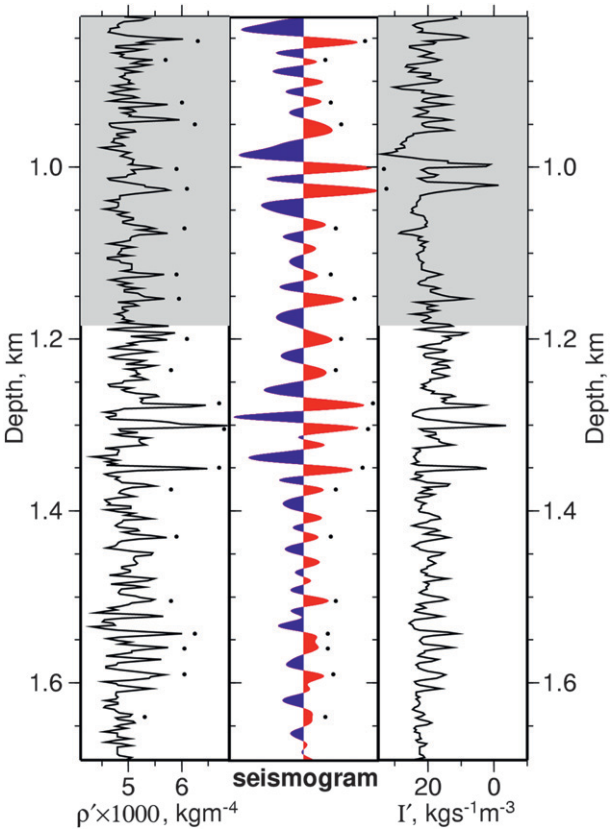

FIG. 3. Analysis of CTD cast acquired on 15 Nov 1994 (see Fig. 1 for location). (left) Vertical gradient of in situ density ρ' calculated in standard way, (right) acoustic impedance I' determined from sound speed and density profiles that were estimated from temperature and salinity measurements, and (middle) seismogram (i.e., acoustic response). Positive (red) and negative (blue) are shown. Seismogram calculated by convolving I' with a Ricker wavelet of central frequency 20 Hz, designed to match the seismic bandwidth of the original seismic experiment (Heigl 2007). Note the good correspondence between peaks on ρ' and the seismogram (black dots). Frequency content of Ricker wavelet limits vertical resolution of seismogram. AAIW mass that is identified by potential density of less than 1027.35 kg m^{-3} is identified (gray band; Arhan et al. 2002). The CTD data were collected using RRS *James Clark Ross* (cruise JR0B) as part of the World Ocean Circulation Experiment and archived by the British Oceanographic Data Centre.

which is perpendicular to the seismic traverse. To estimate geostrophic velocities from the density field, the Coriolis force and any horizontal pressure gradients are assumed to be in equilibrium. This force balance causes tilting of density layers within the water column. On a two-dimensional slice, the vertical shear of horizontal velocity perpendicular to the measured density field is determined from the slope of an isopycnal surface using the standard thermal wind equation (Margules 1906; McWilliams 2006). Thus,

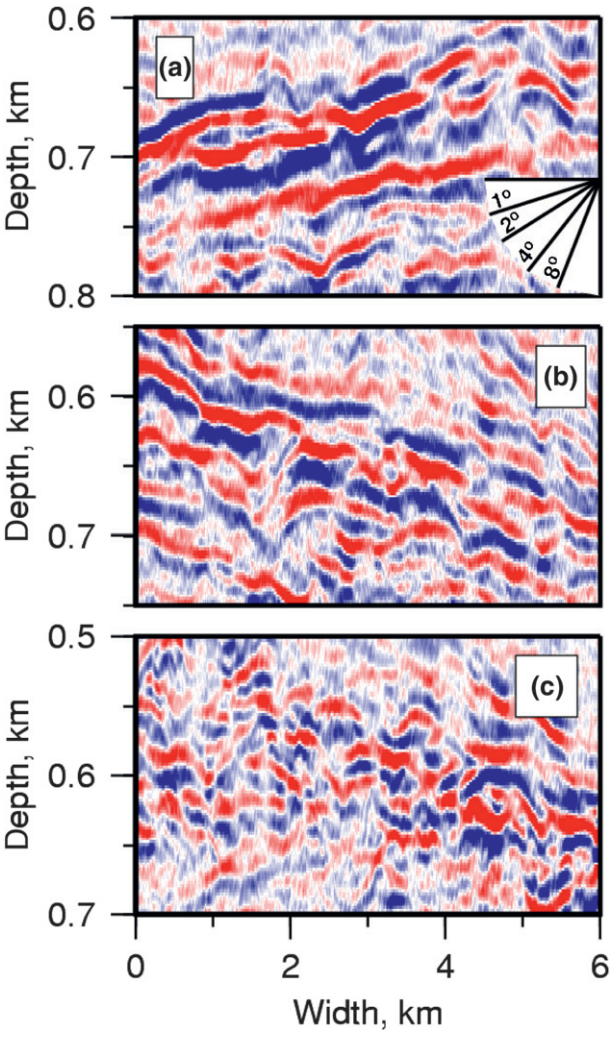

FIG. 4. Three enlarged portions of seismic image (see Fig. 2 for location). In each case, vertical exaggeration is 30 times. (a) Portion located within eastward geostrophic flow. Inset shows values of slope. Vertical shear across box: $\Delta u = +0.07$ m s^{-1}. (b) Portion located within westward geostrophic flow. Vertical shear across box: $\Delta u = -0.08$ m s^{-1}. In both cases, note continuity and slope reversal of reflections. (c) Portion located close to edge of Falkland Trough where diapycnal mixing is enhanced. Note disrupted and undulating reflections, which indicate greater mixing and suggest that geostrophic velocity calculations are no longer valid.

$$\Delta u_i = \frac{g}{f}\left(\frac{\Delta\rho_i}{\rho}\right)\tan\gamma, \qquad (1)$$

where Δu_i is the change in the horizontal component of geostrophic velocity across a density layer interface, f is the Coriolis parameter, g is gravitational acceleration, $\Delta\rho_i$ is the change of in situ density across the interface, ρ is the density of the mixed layer below the interface, and γ is the angle between the interface and the geopotential surface.

The degree to which geostrophic balance applies depends upon the Rossby number Ro = U/fL, where U and L are the characteristic velocity and length scale. If Ro $\ll 1$, the system is dominated by the earth's rotation and is in geostrophic balance. In the Falkland Trough, where $f \sim 10^{-4}$ s^{-1} and $U \sim 0.1$ m s^{-1}, Ro < 0.1 for $L >$ 10 km. This minimum length scale prescribes the way in which a seismic profile should be gridded. We have divided the profile into a series of overlapping boxes which are 12 km wide and 200 m deep.

Within each box, we assume that reflective surfaces approximate isopycnal surfaces. This important assumption is supported by nearby CTD data that show the close correlation of the vertical gradients of in situ density and acoustic impedance (Fig. 3). Krahmann et al. (2009) have shown that isopycnal slopes, measured with a yoyo-CTD probe, match slopes of reflections for periods of up to 4 h. In the Falkland Trough, the vessel steamed at ~2 m s^{-1} so that a 20-km swath of seismic data was acquired within 4 h. These numbers suggest that reflections shorter than 20 km track isopycnal surfaces. Finally, if the inverse slopes of reflections are plotted against the ratio of the local buoyancy frequency N, computed for the nearby CTD cast, to the Coriolis frequency, we find that N/f is an order of magnitude smaller than the inverse slopes. Following Smith and Ferrari (2009), this relationship implies that in the region of interest the effect on density of spatial variations in temperature are not cancelled by those of salinity, which is consistent with, but does not prove, our assumption.

From a physical oceanographic perspective, the dominant frequency of the seismic experiment is low (~20 Hz). Kilometer-scale features are well resolved—an important advantage for geostrophic calculations. Higher-frequency (~80 Hz) seismic experiments produce better images of small-scale ageostrophic structure, but large-scale sloping features are less well resolved (Hobbs et al. 2009).

The average slope of reflective horizons $\langle\tan\gamma\rangle$ is measured in each box. An automated tracking algorithm is used to digitize continuous events (Sheen et al. 2009). Horizons shorter than 2 km were discarded because a 1-km length is equivalent to Ro = 1. Tracking was aborted if the reflective amplitude dropped below the ambient noise threshold. The slope of each tracked horizon was measured and $\langle\tan\gamma\rangle$ was calculated by weighting each tracked event according to its length.

Average slope estimates are used to calculate the difference in geostrophic velocity Δu from the top to the bottom of a box. The change in potential density across a box at a given depth $\Delta\rho_\theta$ is calculated directly from CTD data, which were smoothed and sampled every 100 m. McDougall (1988) has shown that the ratio of the in situ density and potential density changes across a layer interface is given by

$$\mu = \frac{\Delta\rho_i/\rho}{\Delta\rho_{\theta i}/\rho_\theta} = c(R_\rho - 1)/(R_\rho - c), \quad (2)$$

where $\Delta\rho_{\theta i}$ is the potential density change across a single interface, and R_ρ is the stability ratio of the water column; $c = [\alpha(p)/\beta(p)]/[\alpha(p_r)/\beta(p_r)]$ is the ratio of the thermal expansion coefficient α to the saline contraction coefficient β at the in situ pressure p, all of which are divided by the same ratio at a reference pressure p_r. In this way, CTD data are used to calculate μ as a function of depth. In the Falkland Trough, μ is ~1.1.

Equations (1) and (2) yield an estimate of geostrophic shear Δu across a box (i.e., the change in the horizontal component of the geostrophic velocity) where

$$\Delta u = \sum_{\text{box}} \Delta u_i \approx \frac{g}{f}\left(\frac{\mu\Delta\rho_\theta}{\langle\rho_\theta\rangle}\right)\langle\tan\gamma\rangle, \quad (3)$$

where the angle brackets denote the average value across a box. This method is equivalent to summing Δu_i over each box and, crucially, it sidesteps the need to calculate density changes across individual reflections.

Absolute values of geostrophic velocity are determined by integrating Δu over the depth from a level of known motion. An obvious approach exploits velocities obtained from satellite altimetric and acoustic Doppler current profile (ADCP) measurements (Fig. 2c). Here, we used both sets of measurements to estimate the component of velocity that is normal to the seismic profile. Within the trough, satellite altimetric and shipborne ADCP velocity estimates agree. To avoid boundary layer effects, the calculation is stopped 200 m above the seabed.

4. Results

The calculated spatial distribution of absolute current velocity across the Falkland Trough is shown in Fig. 2d. Although we show ADCP-derived velocity values, similar results are obtained if we use satellite altimetric data. The magnitude and direction of the recovered velocity field closely matches the slopes of reflective horizons over length scales of ~10 km. Values are typically ± 0.1 m s^{-1} and in a given box; the error is ± 0.01 m s^{-1}. These errors accumulate downward from the level of known motion. A marked switch in polarity occurs in the center of the trough indicating current reversal within 5–10 km. The integrated east–west baroclinic transport into and out of the trough is $+0.26 \pm 0.14$ and -0.37 ± 0.17 Sv (1 Sv $\equiv$ 10^6 m^3 s^{-1}), respectively. These values are consistent with the analysis of Arhan et al. (2002). Uncertainties in our transport values result from uncertainties in ADCP values that are typically ± 0.05 m s^{-1}.

Similar results have been obtained for other north–south seismic transects shown in Fig. 1. The east–west component of baroclinic velocity decreases toward the east. Along the east–west profile, northward flow is evident but it rapidly decreases toward the western end of the trough.

At the edges of the trough, the seabed shallows to less than 1.2 km [i.e., Ro ~ $O(1)$], and the calculated velocity shear is smaller and in the opposite sense [i.e., the velocity shear has flipped sign, resulting in the velocity at the very edges on the trough increasing (as opposed to decreasing) with depth]. On the acoustic image, disrupted packages of reflectivity slope toward the center of the trough (Fig. 2c). This evidence for ageostrophic flow is supported by elevated diapycnal diffusivities along the trough margins where turbulent mixing is promoted by the breaking of internal waves along the edges of the trough (Fig. 2b; Sheen et al. 2009).

5. Conclusions

We describe a method for estimating geostrophic shear values from seismic profiles. These images record details of oceanic thermohaline structure down to abyssal depths. Our method is based upon slopes of large-scale reflections for which the Rossby number is sufficiently small. It has been applied to a seismic transect, which crosses a significant current loop in the Antarctic Circumpolar Current as it flows over the Falkland Plateau toward the South Atlantic Ocean. In the center of the Falkland Trough where geostrophic balance is expected, the spatial variation of geostrophic shear calculated from the seismic observations has been combined with near-surface ADCP measurements to compute the geostrophic velocity field. Our results are consistent with the overall pattern of reflectivity and with satellite altimetric observations. In water depths shallower than the length scale, which has a Rossby number of ~1 (e.g., the southern margin of the trough), our calculations break down and a highly disrupted reflectivity indicative of enhanced diapycnal diffusivity is observed. The ability to determine the spatial distribution of baroclinic velocities in a direction perpendicular to seismic profiles complements techniques that estimate in-plane current speeds (Klaeschen et al. 2009). Practical application of the technique that we outline would be improved by combining seismic imaging with coeval hydrographic measurements. It would be fruitful to apply our method to three-dimensional seismic data that contain a wealth of spatial and temporal information about oceanic circulation.

Acknowledgments. KLS was supported by the Natural Environment Research Council (NERC) United Kingdom, and by Schlumberger Cambridge Research. We are grateful to WesternGeco for providing the seismic

data and to D. Klaeschen who generously helped KLS to process seismic data at IFM-GEOMAR. We also thank P. Christie, A. Crosby, K. Heywood, R. Jones, D. Koenitz, D. Lyness, M. Meredith, A. Naveira Garabato, C. Richardson, S. Thorpe, and C. Trowell for their help.

REFERENCES

Arhan, M., A. C. Naveira Garabato, K. J. Heywood, and D. P. Stevens, 2002: The Antarctic Circumpolar Current between the Falkland Islands and South Georgia. *J. Phys. Oceanogr.,* **32,** 1914–1931.

Heigl, W. M., 2007: Computing Gaussian derivative waveforms of any order. *Geophysics,* **72,** H39–H42, doi:10.1190/1.2716624.

Hobbs, R. W., D. Klaeschen, V. Sallarès, E. Vsemirnova, and C. Papenberg, 2009: Effect of seismic source bandwidth on reflection sections to image water structure. *Geophys. Res. Lett.,* **36,** L00D08, doi:10.1029/2009GL040215.

Holbrook, W. S., P. Páramo, S. Pearse, and R. W. Schmitt, 2003: Thermohaline fine structure in an oceanographic front from seismic reflection profiling. *Science,* **301,** 821–824.

Klaeschen, D., R. W. Hobbs, G. Krahmann, C. Papenberg, and E. Vsemirnova, 2009: Estimating movement of reflectors in the water column using seismic oceanography. *Geophys. Res. Lett.,* **36,** L00D03, doi:10.1029/2009GL038973.

Koenitz, D., N. White, I. N. McCave, and R. W. Hobbs, 2008: Internal structure of a contourite drift generated by the Antarctic Circumpolar Current. *Geochem. Geophys. Geosyst.,* **9,** Q06012, doi:10.1029/2007GC001799.

Krahmann, G., C. Papenberg, P. Brandt, and M. Vogt, 2009: Evaluation of seismic reflector slopes with a Yoyo-CTD. *Geophys. Res. Lett.,* **36,** L00D02, doi:10.1029/2009GL038964.

Margules, M., 1906: Über Temperaturschichtung in stationär bewegter und ruhender Luft. *Hann-Band. Meteor. Z.,* **23,** 243–254.

McDougall, T. J., 1988: Neutral-surface potential vorticity. *Prog. Oceanogr.,* **20,** 185–221.

McWilliams, J. C., 2006: *Fundamentals of Geophysical Fluid Dynamics*. Cambridge University Press, 266 pp.

Ruddick, B., H. Song, C. Dong, and L. Pinheiro, 2009: Water column seismic images as maps of temperature gradient. *Oceanography,* **22,** 192–205.

Sallarès, V., B. Biescas, G. Buffett, R. Carbonell, J. J. Dañobeitia, and J. L. Pelegri, 2009: Relative contribution of temperature and salinity to ocean acoustic reflectivity. *Geophys. Res. Lett.,* **36,** L00D06, doi:10.1029/2009GL040187.

Sheen, K. L., N. J. White, and R. W. Hobbs, 2009: Estimating mixing rates from seismic images of oceanic structure. *Geophys. Res. Lett.,* **36,** L00D04, doi:10.1029/2009GL040106.

Sherwin, T., S. L. Hughes, W. R. Turrell, B. Hansen, and S. Østerhus, 2008: Wind-driven monthly variations in transport and the flow field in the Faroe-Shetland Channel. *Polar Res.,* **27,** 7–22, doi:10.1111/j.1751-8369.2007.00036.x.

Smith, K. S., and R. Ferrari, 2009: The production and dissipation of compensated thermohaline variance by mesoscale stirring. *J. Phys. Oceanogr.,* **39,** 2477–2501.

Zenk, W., 1981: Detection of overflow events in the Shag Rocks Passage, Scotia Ridge. *Science,* **213,** 1113–1114.